Improvement of grain alignment in $Bi_2Sr_2Co_{1.8}O_y$ thermoelectric through the electrically assisted laser floating zone

N.M. Ferreira[1], M.A. Madre[2], M. A. Torres[2], A. Davarpanah[3], V. Amaral[3], F.M. Costa[1], A. Sotelo[2]

[1]i3N, Departamento de Física, Universidade de Aveiro, 3810-193 Aveiro, Portugal.

[2]ICMA (CSIC-Universidad de Zaragoza), Dpto. de Ciencia de Materiales, C/María de Luna 3, 50018-Zaragoza (Spain).

[3]CICECO – Aveiro Institute of Materials, Universidade de Aveiro, 3810-193 Aveiro, Portugal.

Abstract

Thermoelectric performances of cobaltite ceramics were improved by increasing grain sizes and alignment through the Electrically Assisted Laser Floating Zone method. $Bi_2Sr_2Co_{1.8}O_y$ ceramics were directionally grown at 30 mm/h, applying external DC (0-500 mA) during the growth process. Microstructure and thermoelectric properties are significantly influenced by the external current direction and intensity. Negative currents/pole on the seed rod prevent the formation of thermoelectric phase, while positive pole on the seed rod, decreases the amount of secondary phases and increases grain orientation when compared to samples grown without current. Annealing procedure decreases secondary phases content, without modifying grain alignment. The best thermoelectric performances were obtained for samples grown with +300 mA , reaching the highest ZT values of 0.09 at 650 ºC. Moreover, it should be highlighted that these processed samples can be directly applied in thermoelectric modules, avoiding the long and expensive steps necessary when other preparation processes are used.

Keywords

Bi-Sr-Co-O, oxide thermoelectric, Electrically Assisted Laser Floating Zone, thermoelectric performance, figure of merit, texture, thermal conductivity

1. Introduction

Nowadays, the reduction of CO_2 emissions is one of the main objectives considered in the scientific strategies of many countries, not only due to their influence on global warming but also for the associated wasted energy. In this regard, thermoelectric (TE) materials are notice to increase the efficiency of fossil fuel engines, through harvesting their wasted heat and transforming it into useful electrical energy [1]. Currently, commercial thermoelectric modules are built using metallic alloys or intermetallic compounds. These materials are characterized by high thermoelectric performances at moderate temperatures [2], which are evaluated through the dimensionless figure-of-merit: ZT=S2 T/ρκ; where, S: Seebeck coefficient, T: absolute temperature, ρ: electrical resistivity and κ: thermal conductivity [3]. On the other hand, they usually contain heavy metals, which are characterized by low chemical stability at high temperatures under air atmosphere, low abundance in the earth crust, and toxic nature. Consequently, the applications to recover waste heat coming from high temperature heat sources remains unexploited. For this purpose, oxide materials have been considered as a promising alternative in these working conditions [4]. Despite oxide-based material exhibit relatively low performances, their ceramic nature provides high chemical and thermal stability at high temperatures. Moreover, they are composed of abundant and cheaper elements than intermetallic compounds.

Among these ceramic materials, the highest performances have been achieved in CoO-based families, with p-type semiconducting behavior [5–7], and MnO- and TiO-based ones, as n-type [8–10]. Particularly, the crystalline structure of CoO-based materials can be described through a monoclinic cell composed of two different subcells alternatively stacked. These are a conducting CoO_2 layer with CdI_2-type structure, and an insulating one with rock-salt structure. These two subcells are characterized by common a- and c- parameters and β angles, while they differ in the b-parameter values, which produce a misfit structure along this direction [11]. As a consequence of this crystalline anisotropy, it is easy to deduce that appropriate grain alignment can lead to a drastic decrease in electrical resistivity, as previously reported as desired for this type of application [12,13]. To obtain well-aligned grains along the electrical conduction direction, several techniques have been widely used, namely hot-pressing [12], edge-free spark plasma sintering (SPS) [14], laser floating zone (LFZ) [15], reactive templated grain growth (RTGG) [16] or electrically assisted laser floating zone (EALFZ) [17]. Specifically, the EALFZ technique appears as a modification of the LFZ one, when a DC signal is passing through the molten zone during the growth process. Previous works have shown that this modification can drastically improve the grain alignment by decreasing the radial thermal gradient in the solidification front and, consequently, the electrical transport properties in anisotropic ceramic systems are substantially increased [17–19].

The objective of this work is producing textured $Bi_2Sr_2Co_{1.8}O_y$ thermoelectric ceramics through the EALFZ technique using different applied electrical DC intensities and polarities. On the other hand, it should be pointed out that these materials show incongruent melting, which leads to the formation of secondary phases during the solidification step. Consequently, the as-grown materials should be annealed to produce nearly single-phase bulk textured materials. These annealed samples will be

characterized to determine the effect of current intensity and polarity on their microstructural features, which will be related to their thermoelectric performances.

2. Experimental procedure

$Bi_2Sr_2Co_{1.8}O_y$ compounds have been prepared from commercial Bi_2O_3 (99 %, Panreac), $SrCO_3$ (99 %, Panreac), and CoO (99.99 %, Aldrich) powders via the classical solid-state method. The powders were weighed in the stoichiometric proportions and ball milled at 300 rpm for 30 min in water media. The slurry was then dried under infrared radiation, followed by manual milling to break the agglomerates. This homogeneous mixture was thermally treated twice, at 750 and 800 °C for 12 h, with intermediate manual milling, to decompose the $SrCO_3$, avoiding its presence in the next processing steps. The resulting powder was used to produce cylindrical rods, through cold isostatic pressing at 200 MPa (~ 3mm diameter and 100mm length), which have been used as feed in an EALFZ system equipped with a continuous CO_2 laser (λ =10.6 μm) [17]. The melt-solidification process has been performed using 30 mm/h growth rate for all samples, and different applied electrical DC intensities: 0, +100, +200, +300, +400, +500, and -400 mA. The sign before the values of the current indicates the electrical pole connected to the seed during the growth process [17]. The samples grown without applied electrical current (0 mA) will be used as a reference. After the production of geometrically homogeneous long rods (> 100 mm), they were cut into ~ 15mm long pieces. As it has been previously indicated, due to the incongruent melting of these materials, some as grown samples were annealed at 810 °C for 24 h, with a final furnace cooling to significantly reduce the secondary phases content.

Powder XRD analysis has been performed on crushed samples using a Philips X'Pert MRD equipment between 5 and 70 degrees to identify the different phases. Pole figures, performed on transversal sections, were obtained using the (200) diffraction plane to determine the grain orientation [18]. The Lotgering factor (f) was also calculated to estimate the orientation degree of crystallites. This factor is calculated based on the diffraction peak intensities of XRD patterns of bulk samples, according to the following equation:

$$f = \frac{(p_x - p_0)}{(1 - p_0)} \quad (1)$$

considering,

$$p_x = \frac{\sum I_{(001)}}{\sum I_{(113)}} \quad (2)$$

p_x is the intensity ratio of the (001) and (113) diffractions of samples grown with applied current (100, 200, 300, 400, 500 and –400 mA). p_0 is similarly defined for the 0 mA sample (without current) [18].

The microstructure has been studied on polished longitudinal sections of samples in a FESEM (Zeiss Merlin), with an EDS system used to determine the qualitative composition of the different phases. Electrical resistivity and Seebeck coefficient were simultaneously determined along the fibres growth direction, using the four-point

method under steady-state conditions, between 50 and 650 °C, using an LSR-3 device (Linseis GmbH).

Thermal conductivity has been measured in bulk samples, along the fibres growth direction, at room temperature (RT) using the transient plane source technique (Hot Disk TPS 2500s). The thermoelectric performances of the different samples (ZT) have been calculated at RT and estimated for higher temperatures using the κ values at RT. It is necessary to highlight that most of the reports available in the literature show that κ values are not significantly affected when the temperature is increased, exhibiting usually a slightly decrease [19–25].

3. Results and discussion

3.1. As-Grown samples

Representative powder XRD patterns of as-grown samples are presented in Fig. 1a. In all cases, the most intense peaks have been assigned to the $Bi_2Sr_2Co_{1.8}O_y$ thermoelectric phase (identified by their diffraction planes) [13,17,26]. On the other hand, it can be observed that external electrical DC promotes modifications in these patterns. The samples grew without applied current present a large number of phases and, in agreement with previous works in this system [13,26,27], these diffractions can be attributed to Sr-Bi-O, Bi-Sr-Co-O, Bi poor Bi-Sr-Co-O and Co-O phases.

When positive external currents are applied, the diffraction peak intensities of these secondary phases are reduced, indicating a larger content of thermoelectric phase. This reduction of secondary phases can be associated with the extra energy applied to the system through the electrical DC, which promotes the preferential crystallization of the TE phase. Similar behaviour was already observed in High-T_c superconductors processed by this technique [28]. On the other hand, the use of negative external current hinders the thermoelectric phase crystallization and, consequently, increases the secondary phases peak intensities. The raise of secondary phases content is a clear indication that this polarity in the electrical current prevents the thermoelectric phase formation, in agreement with previous results in the $Bi_2Ca_2Co_{1.7}O_y$ system [17]. These differences can be explained from an electrochemical point of view, through the interaction between the ions electrical charge and the polarity of the external electrical field [17].

The values of Lotgering factor (Fig. 1b) evidence an increase of grain orientation with the applied current intensity, obtaining a maximum for 400 mA. The use of negative external current prevents texture, even when compared to the fibre grown without current (0 mA), as expected from previous results [17].

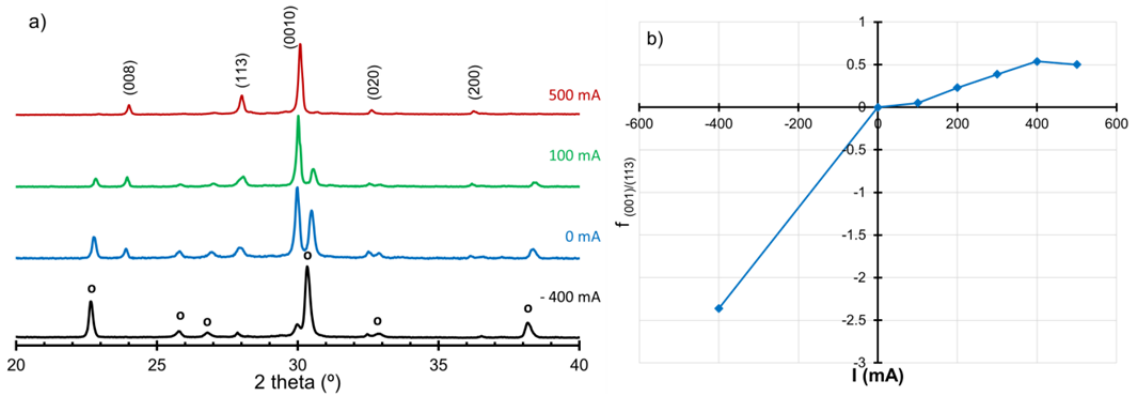

Fig. 1. a) Powder XRD patterns of $Bi_2Sr_2Co_{1.8}O_y$ samples grown under different applied currents. The diffraction planes identify the $Bi_2Sr_2Co_{1.8}O_y$ phase diffraction peaks, while minor ones (o) correspond to unidentified secondary phases; b) Lotgering factor using (001) and (113) planes of samples grown with different applied current intensities.

Representative micrographs of samples grown with different currents and polarities are displayed in Fig. 2. In these micrographs, it can be observed that samples are formed by a large amount of secondary phases, especially those grown with – 400 mA, corroborating the XRD data previously discussed. The image of the sample grown with negative current (Fig. 2a) shows 3 different contrasts (identified by arrows and numbers), which correspond to different compositions, obtained through EDS analysis. These are, white (#1, aligned Bi-Sr-O), black (#2, dendritic CoO), and light grey (#3, aligned $Bi_2Sr_2Co_{0.9}O_x$, 221) contrasts. Moreover, no thermoelectric phase has been identified in this sample, as previously observed in similar systems [17]. On the other hand, besides these secondary phases, two new ones have been identified in samples grown without current (Fig. 2b), dark grey (#4, Bi-poor Bi-Sr-Co-O), and medium grey (#5, thermoelectric phase). The presence of these phases is in agreement with previous results in this system [13,26,29]. The qualitative composition of each phase, obtained through EDS measurements is displayed in Table 1.

Table 1. Mean elemental phase composition (at.%) and standard deviation obtained with EDS analysis

Number/Phase	Sr	Bi	Co	O
1. (Bi+Sr)O	12.75 (±2.01)	28.85 (±2.26)		58.09 (±1.12)
2. CoO_x			48.67 (±0.93)	51.33 (±0.93)
3. 221	16.92 (±0.68)	19.14 (±0.65)	8.19 (±0.39)	55.76 (±0.97)
4. $Sr_2Co_{2.8-x}Bi_xO_y$	19.57 (±0.52)	4.26 (±0.32)	20.76 (±1.47)	55.41 (±2.19)
5. 222 (TE)	14.67 (±0.16)	15.80 (±0.27)	12.95 (±0.32)	56.59 (±0.60)

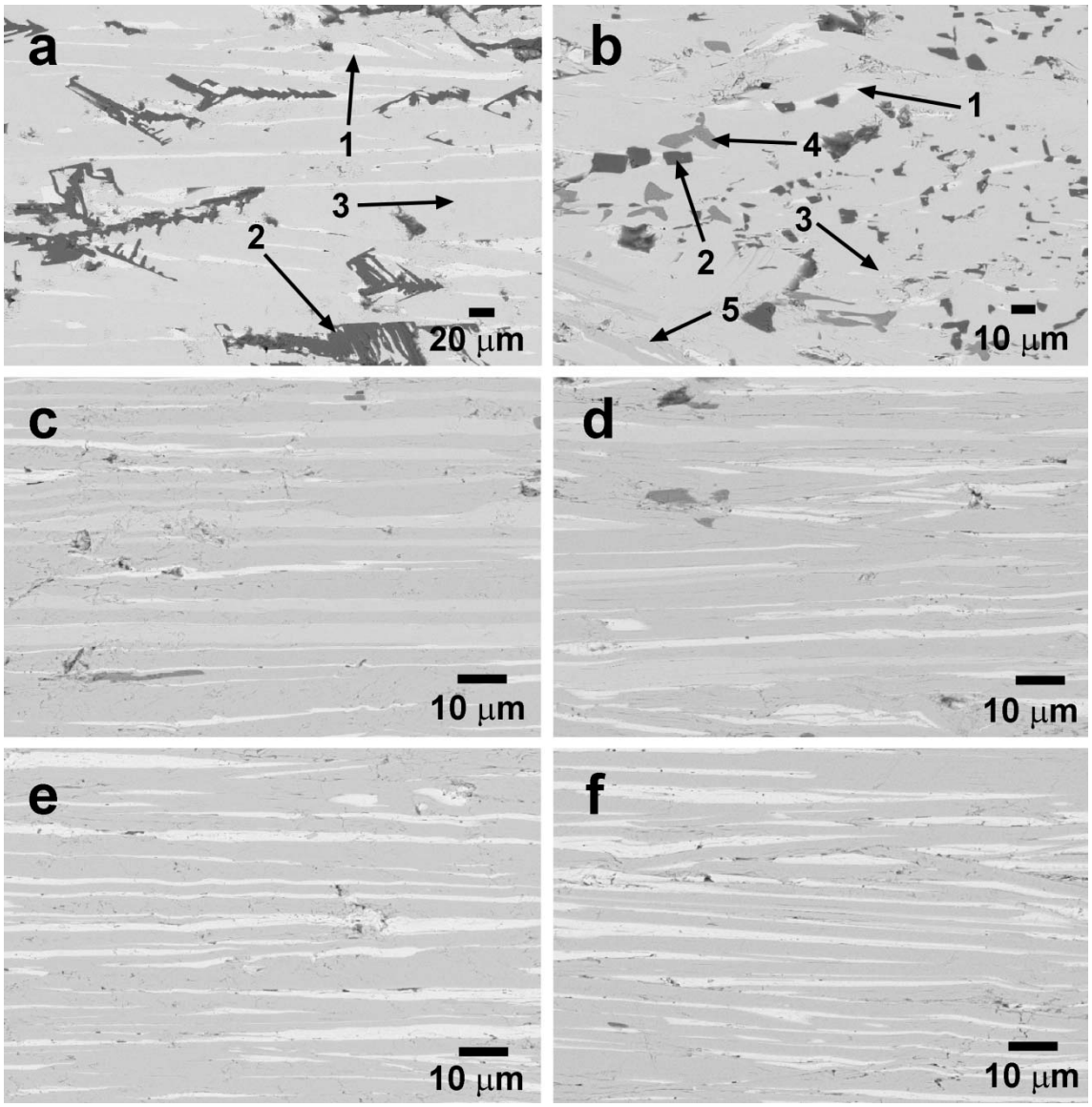

Fig. 2. Micrographs of as-grown $Bi_2Sr_2Co_{1.8}O_y$ samples, a) with negative current (-400 mA); b) without current; and with positive current: c) +200, d) +300, e) +400, and f) +500mA. The arrows identify the different contrasts and the numbers show the phases identified with EDS analysis: 1) Bi-Sr-O; 2) CoO; 3) $Bi_2Sr_2Co_{0.9}O_x$; 4) Bi-poor Bi-Sr-Co-O; and 5) $Bi_2Sr_2Co_2O_y$.

When positive current is used during the growth process, the number and amount of secondary phases decrease when the applied intensity is raised. The fibres grown with +100 mA (not shown) are very similar to those grown without current due to the low electrical field, which is not enough to significantly modify cations mobility. However, when the intensity is higher, the CoO phase disappears, while the Bi-poor Bi-Sr-Co-O and 221 phases content are reduced. These two phases were not identified through XRD since no XRD database has matched to these peaks. At the same time, the grain sizes and alignment are drastically improved, leading to a much lower number of grain boundaries along the growth direction [26].

In Fig. 3, the electrical resistivity evolution with temperature is presented. As it can be easily observed, all samples present semiconducting behaviour ($d\rho/dT<0$) in the measured temperature range. As it can be observed, the highest values have been determined in samples grown with -400 mA, which is coherent with the absence of thermoelectric phase in these samples. On the other hand, the electrical resistivity is decreased when the positive current intensity is increased, when compared to the one obtained in samples grown without current. This evolution reflects the microstructural modifications previously discussed. The minimum values at 650 °C (8.7 mΩ cm), obtained in samples grown with +500 mA, are much lower than the reported in sinter-forged textured materials (40 mΩ cm) [30], or in sintered specimens under oxygen (15 mΩ cm) [31].

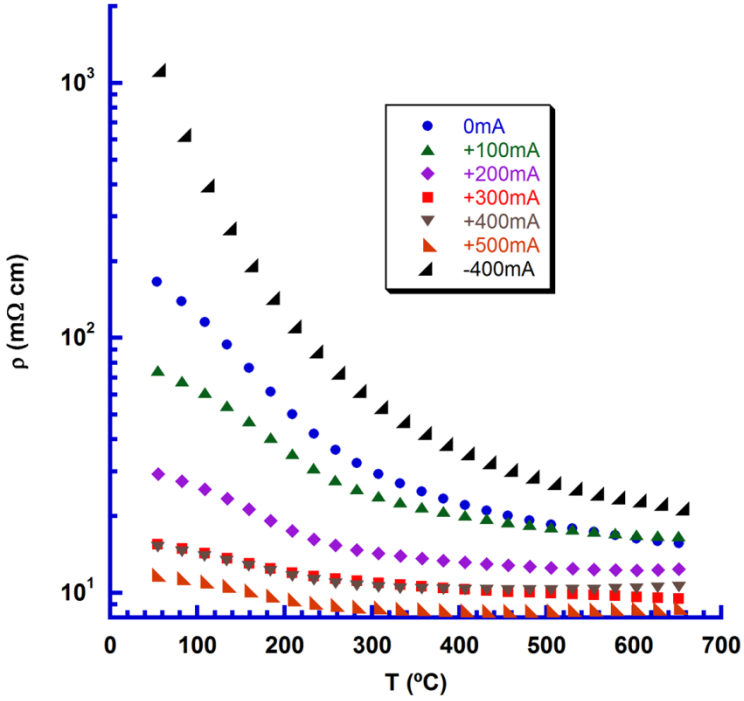

Fig. 3. Evolution of electrical resistivity of samples with temperature, as a function of the external applied DC intensity.

Seebeck coefficient, S, evolution with temperature is displayed in Fig. 4 for all samples. S values are positive in the whole measured temperature range, indicating a dominating hole transport mechanism. As it can be expected, samples grown with -400 mA display the lowest values because no thermoelectric phase has been produced. On the other hand, the values for the other samples at room temperature are very similar, being slightly higher for samples grown with applied current. When observing S behavior with temperature, it is easy to deduce that current intensity plays an important role, clearly modifying S values evolution. The highest S value at 650 °C has been determined in samples grown with +400 mA (142 μV/K), which is only slightly lower than the one obtained in sinter-forged materials (150 μV/K) [30], but much lower than the reported in samples produced through solution methods (205 μV/K) [32].

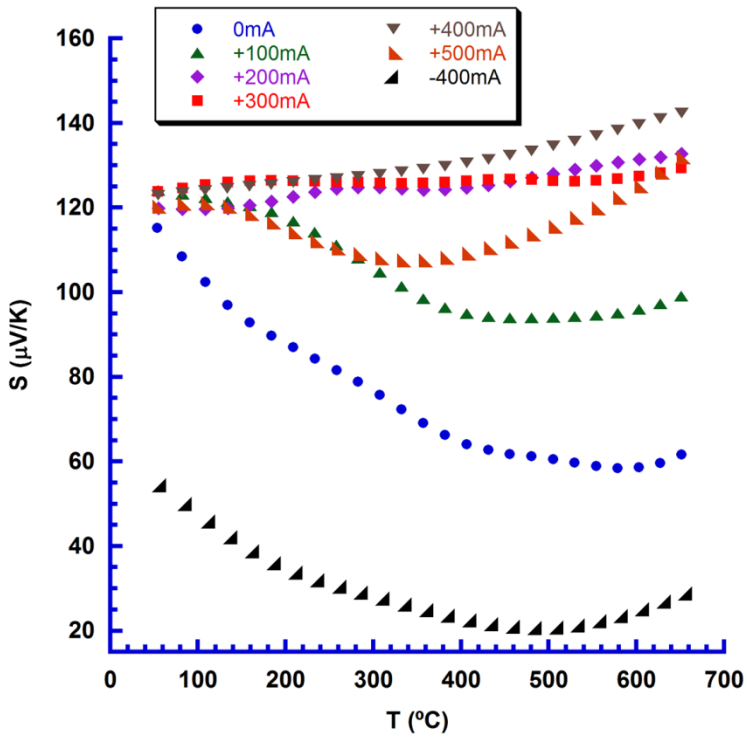

Fig. 4. Evolution of the Seebeck coefficient of samples with temperature, as a function of the external applied DC intensity.

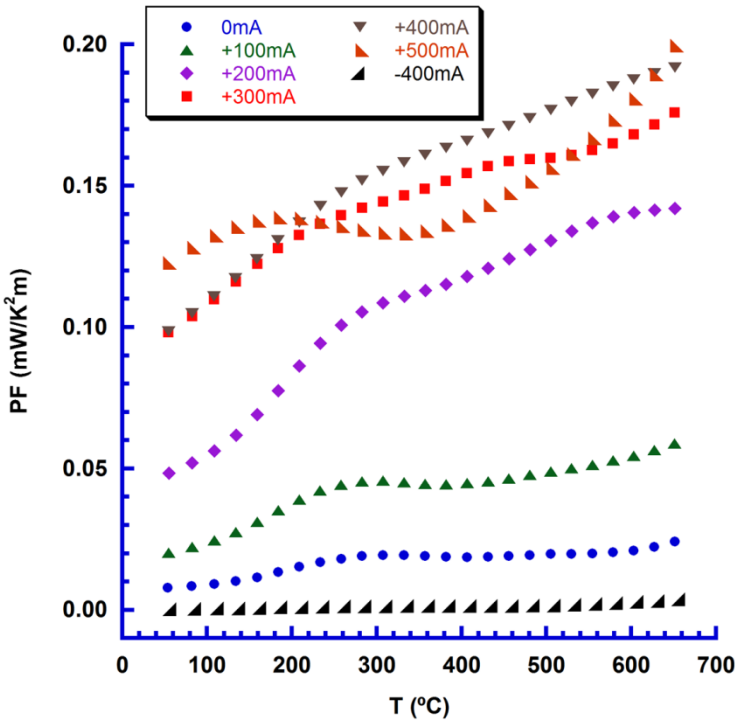

Fig. 5. Evolution of PF with temperature, as a function of the external applied DC intensity.

Using the electrical resistivity and Seebeck coefficient data, power factor ($PF = S^2/\rho$) has been calculated and displayed in Fig. 5. PF significantly increases with electrical

intensity, from -400 to +500 mA at room temperature. The differences between samples can be due to the effect of current intensity on the oxygen content, and vacancies distribution in the crystal structure [33]. It is important to highlight that the very low PF values determined for samples grown with -400 mA, in the whole measured temperature range, is due to the absence of the TE phase in the bulk material. The highest PF values at 650 °C have been measured in samples grown with +400 and +500 mA (~ 0.20 mW/K^{2}m), which are similar to the measured in samples produced by solution methods (0.20 mW/K^{2}m) [32], but much higher than the ones measured in sinter-forged materials (0.05 mW/K^{2}m) [30].

Despite the relatively high PF determined at 650 °C, all samples present a very irregular evolution of S with temperature. This fact, together with the semiconducting behaviour of samples, displaying high electrical resistivity values at room temperature, can be associated to the effect of microstructure (a mixture of several phases), and the oxygen vacancies, on the electrical properties of these materials. Consequently, an annealing procedure can be useful to promote the formation of equilibrium phases and decrease the amount of oxygen vacancies, leading to an increase of thermoelectric performances, as previously reported [26]. This procedure has only been performed on samples grown without, or with positive currents, as they show much lower content, and smaller, secondary phases than those grown with negative intensity, which would need much longer annealing time to produce nearly single TE phase.

3.2. Annealed samples

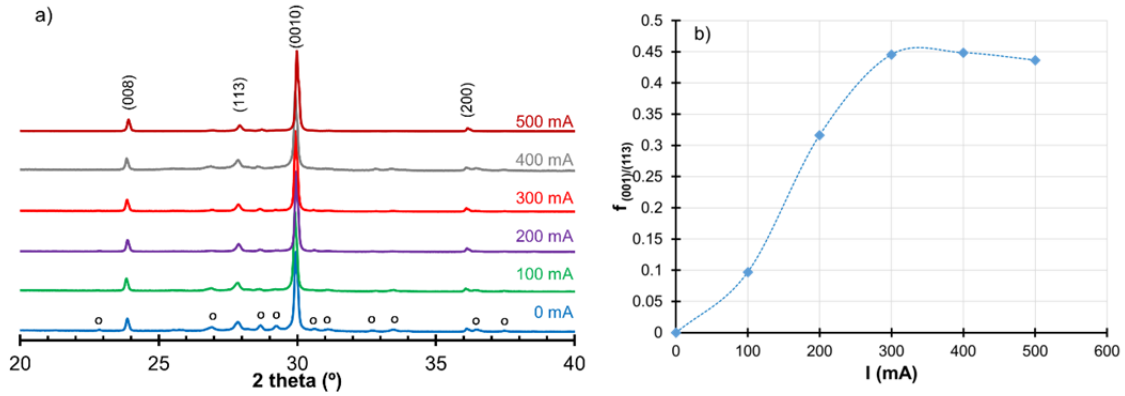

Fig. 6. a) Powder XRD patterns of $Bi_2Sr_2Co_{1.8}O_y$ annealed samples grown under different applied DC intensities. The diffraction planes identify the peaks corresponding to the $Bi_2Sr_2Co_{1.8}O_y$ phase. Peaks shown with (o) indicate unidentified secondary phases. b) Lotgering factor calculated on the (001) and (113) planes for annealed samples grown using different DC intensities.

Powder XRD analysis has been performed in all samples after annealing, and the results are shown in Fig. 6a. In this graph a significant decrease of the secondary phases content can be observed, when compared to the as-grown materials (see Fig. 1a), in agreement with previous works [13,26]. Moreover, the low amount of secondary phases is further decreased when the applied current intensity is increased, with the

additional advantage of improved grain orientation, according to the Lotgering factor (Fig 6b). These results were expected, as they were already discussed in the as-grown materials. However, the best orientation has been obtained for samples grown with +300 mA after annealing.

These results have been corroborated with the SEM observations, as shown in Fig. 7, where representative micrographs are presented. Samples were grown without current present three different contrasts (instead of the five observed in the as-grown samples, see Fig. 2), which are the same observed in samples grown with positive current, as reflected in Table 2. Grey contrast corresponds to the thermoelectric phase, which is the major one in all cases. White contrast is the Bi-poor: Bi-Sr-Co-O phase, while dark grey (Bi-Sr-O) is present in very small proportions. These observations indicate that the annealing process allows a drastic reduction of the secondary phases, obtained in as-grown materials, without modifying grain alignment. It should be noticed that Bi-poor Bi-Sr-Co-O phase has not been identified in the XRD pattern since this phase, has similar peak positions to the thermoelectric phase.

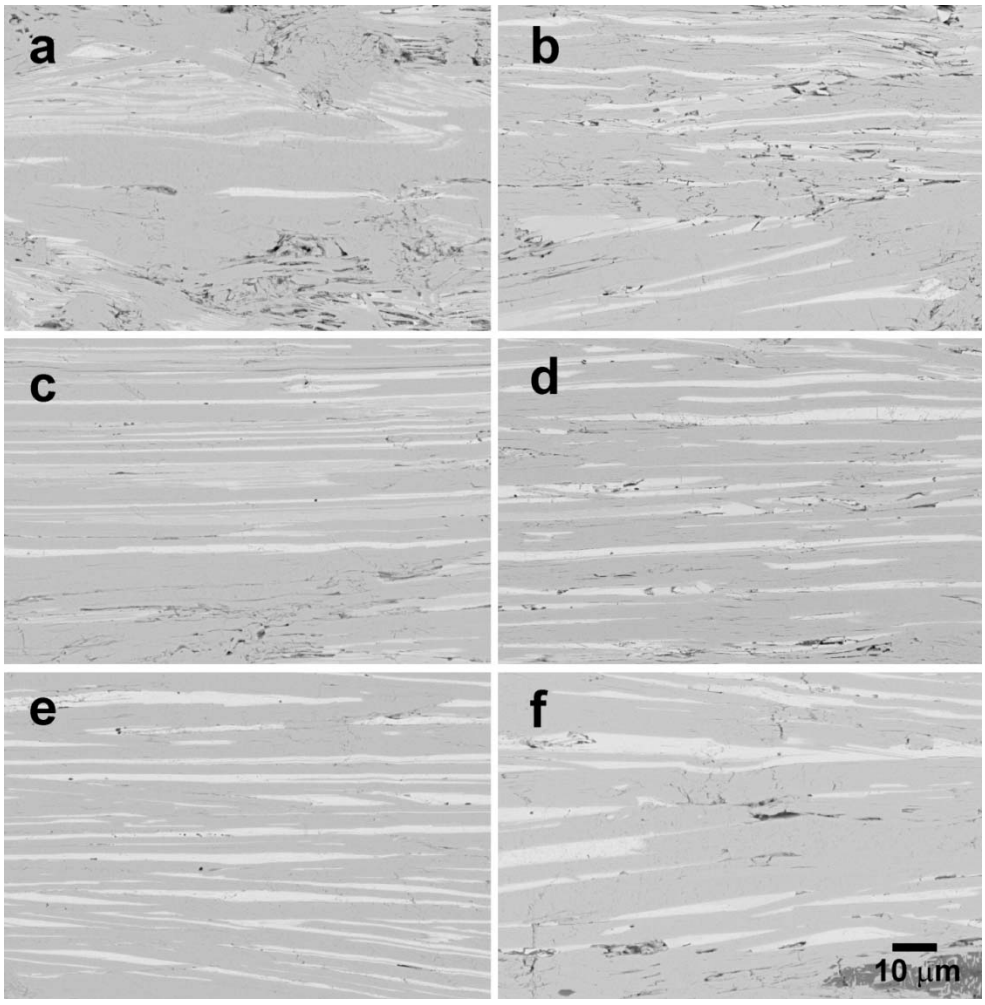

Fig. 7. Micrographs of $Bi_2Sr_2Co_{1.8}O_y$ annealed samples grown with different current intensities, a) 0; b) +100; c) +200; d) +300; e) +400; and f) +500 mA. The three contrasts correspond to thermoelectric phase (grey), Bi-poor Bi-Sr-Co-O (white), and Bi-Sr-O (dark grey).

Table 2. Mean elemental phase composition (at.%) and standard deviation from EDS analysis on annealed fibers

Phase	Sr	Bi	Co	O
(Bi+Sr)O	15.04 (±2.06)	25.73 (±3.37)		58.07 (±0.94)
221	16.55 (±0.50)	19.86 (±0.65)	8.35 (±0.51)	55.25 (±1.10)
222 (TE)	14.40 (±0.35)	15.58 (±0.39)	12.58 (±0.78)	57.45 (±1.41)

Representative pole figures obtained on the transversal section of samples are shown in Fig. 8. In these graphs, it is possible to observe an increase of grain orientation, not only with the applied DC intensity but also with the annealing procedure. These features observed in Fig. 8 for samples grown with 0, and +300 mA can be extended to all samples, as it can be seen in Table 3, where the relative grain alignment is shown. Moreover, from the data presented in Table 3, it is easy to see that the best grain orientation is produced in +300 mA grown samples, confirming the rough analysis from the Lotgering factors previously determined in as-grown and annealed samples (Figs. 1b and 6b).

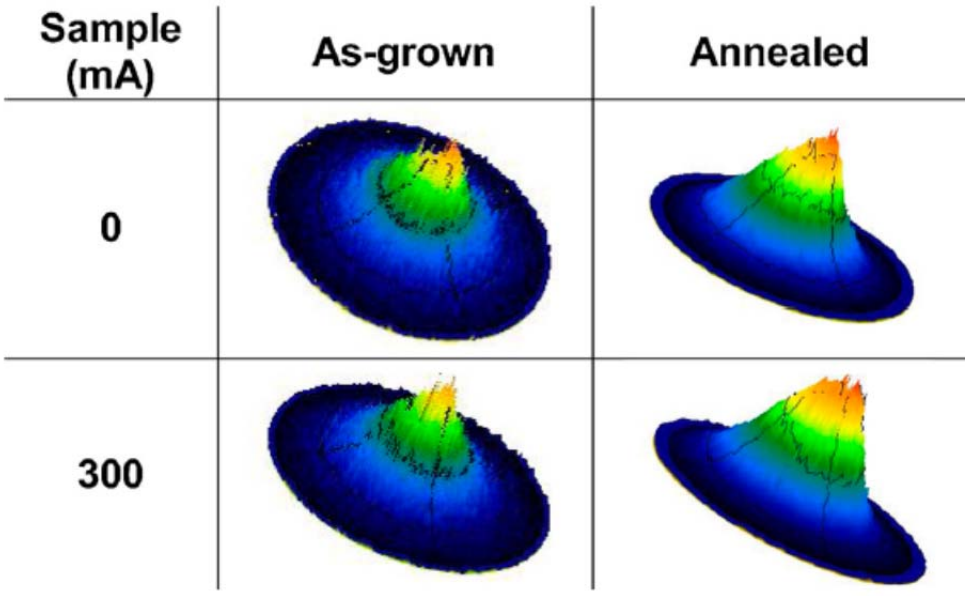

Fig. 8. Representative pole figures of as-grown and annealed samples

Fig. 9 illustrates the electrical resistivity evolution with temperature in annealed samples, as a function of the applied DC intensity. In the graph, it can be observed that annealing leads to a drastic behaviour change from semiconducting ($d\rho/dT<0$, in as-grown samples, see Fig. 3) to metallic ($d\rho/dT>0$) after annealing. Moreover, room temperature resistivity values are decreased with the annealing procedure. Regardless of this decrease, the metallic behaviour leads to higher resistivity values at 650 °C than

those measured in as-grown ones. The lowest electrical resistivity values at this temperature have been determined in +300, and +400 mA grown samples (13 mΩ cm), which are still lower than those reported in sinter-forged textured materials (40 mΩ cm) [30], or sintered specimens under oxygen (15 mΩ cm) [31], even if they are higher than the best values observed in as-grown samples in this work (8.7 mΩ cm).

Table 3. Relative grain alignment of as-grown and annealed samples, obtained from XRD texture measurements

Current (mA)	As- grown	Annealed
0	1.00	1.32
100	0.95	1.43
200	0.94	1.36
300	1.12	1.39
400	1.02	1.22
500	1.06	1.29

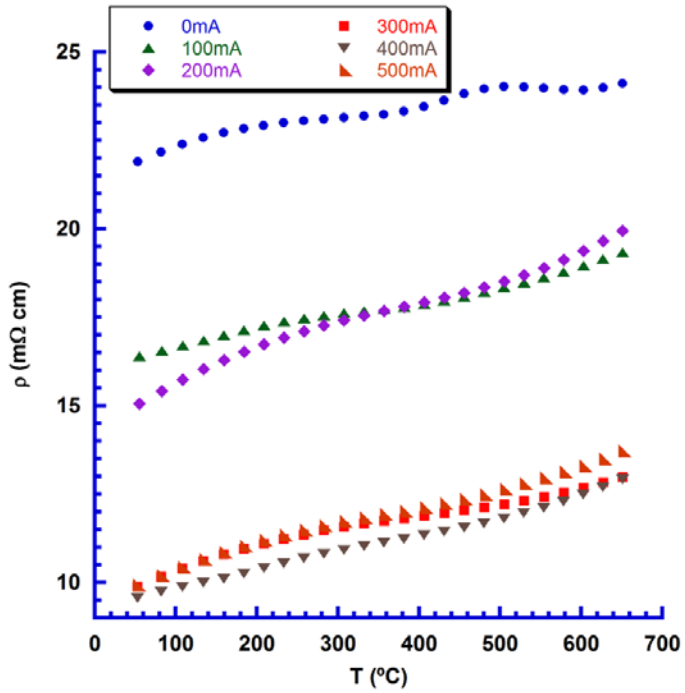

Fig. 9. Electrical resistivity evolution with temperature for annealed samples grown under different DC intensities.

Fig. 10 illustrates the variation of Seebeck coefficient with temperature as a function of the applied DC intensity. The sign of S is positive in the whole measured temperature range, indicating that annealing has not modified the type of charge carriers. On the other hand, no significant variation of S with the applied current can be observed; consequently, the amount of thermoelectric phase and oxygen content are, approximately, the same for all samples. This effect is due to the annealing procedure,

which allows filling the non-equilibrium oxygen vacancies in the bulk material, neglecting the electrical intensity effect on the oxygen vacancies concentration. The highest values at 650 °C (175 μV/K) are much higher than the one obtained in as-grown materials in this work (142 μV/K), and the one observed in sinter-forged materials (150 μV/K) [30], but much lower than the one reported in samples produced through solution methods (205 μV/K) [32].

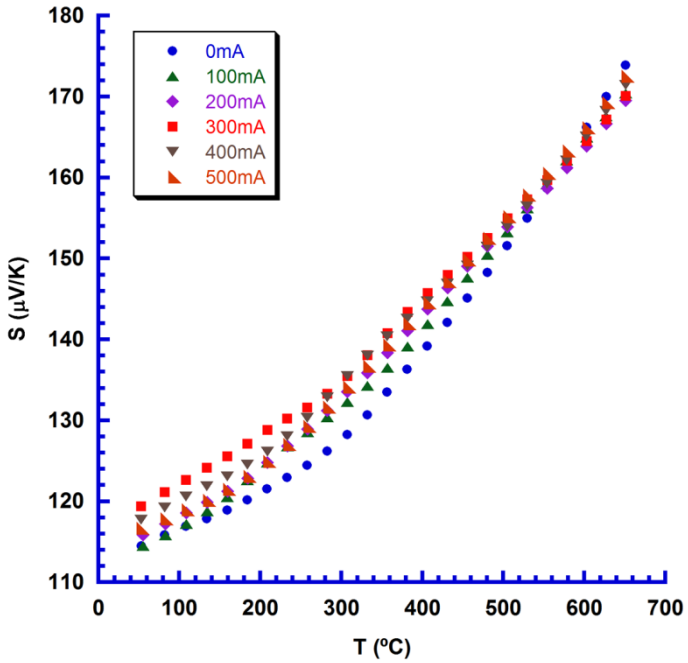

Fig. 10. Seebeck coefficient evolution with temperature for annealed samples grown under different DC intensities.

The electrical performances of samples, evaluated through their PF values, are presented, as a function of temperature, in Fig. 11 for all annealed samples. Room temperature values of these samples are higher (more than 50 %, in most cases) than the determined in as grown ones (see Fig. 5). The highest PF values at 650 °C have been measured in samples grown with +400 mA (0.23 mW/K^2m), which are only slightly higher than the measured in as-grown or annealed materials [34] or even in samples produced by solution methods (0.20 mW/K^2m) [30], but much higher than the ones measured in sinter-forged materials (0.05 mW/K^2m) [30]. This relatively small increase of PF with temperature is mainly due to the metallic behaviour of electrical resistivity in annealed samples.

Table 4 presents the room temperature thermal conductivity of samples. The values are within the reported for this system and displayed in Table 5. These values are decreased when the applied DC is increased up to +300 mA, while higher intensities lead to an increase in thermal conductivity. These results indicate a decrease of phononic thermal conductivity up to +300 mA, since κ can be expressed by the sum of phononic component (κ_{ph}) and mobile electronic carriers' component (κ_e), which can be expressed as $\kappa_e = L\sigma T$, where L, σ, and T are Lorenz number (2.45×10^{-8} V^2/K^2), electrical conductivity, and absolute temperature, respectively [35]. As it has been

previously discussed, the annealed samples grown at +300 mA present the lowest electrical resistivity. Nevertheless, these samples display the lowest thermal conductivity, clearly indicating that passing a DC during the growth process can effectively increase phonon scattering, playing a major role in thermal conductivity [36].

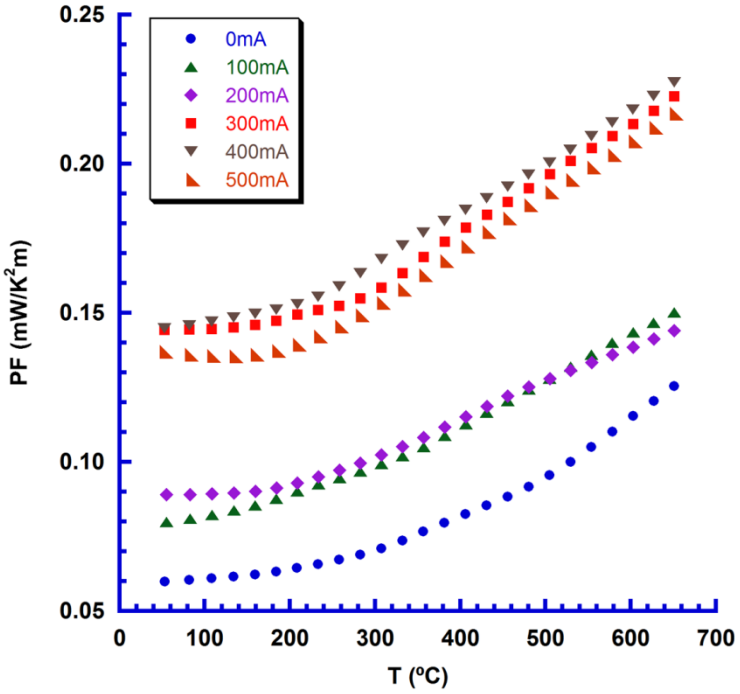

Fig. 11. PF evolution with temperature for annealed samples grown under different DC intensities.

Table 4. Room temperature thermal conductivity of annealed samples grown with different DC intensities.

Sample (mA)	κ (W/m K)
0	2.87
100	2.73
200	2.45
300	2.44
400	2.70
500	2.75

ZT values have been calculated using the previous data, between room temperature and 650 °C, considering κ values unchanged with temperature. The evolution of ZT with temperature as a function of the electrical DC intensity during the growth process is presented in Fig. 12. As it can be easily observed in the graph, the highest values have been determined in samples grown with +300 mA in the whole measured temperature range, reaching the maximum (~ 0.09) at 650 °C. The highest values obtained in this work are much higher than the ones reported for $Bi_2Sr_{2-x}Ca_xCo_2O_y$ system (0.009 at RT) [37], $Bi_2Sr_2Co_2O_y$ prepared under high magnetic field (0.01 at RT)

[38], and slightly lower than that obtained in thin films (0.09 at 150 °C) [39]. On the other hand, these values are very low when compared with Bi-Sr-Co-O/Ag composites (0.26 at 700 °C) [40], as summarized in Table 5.

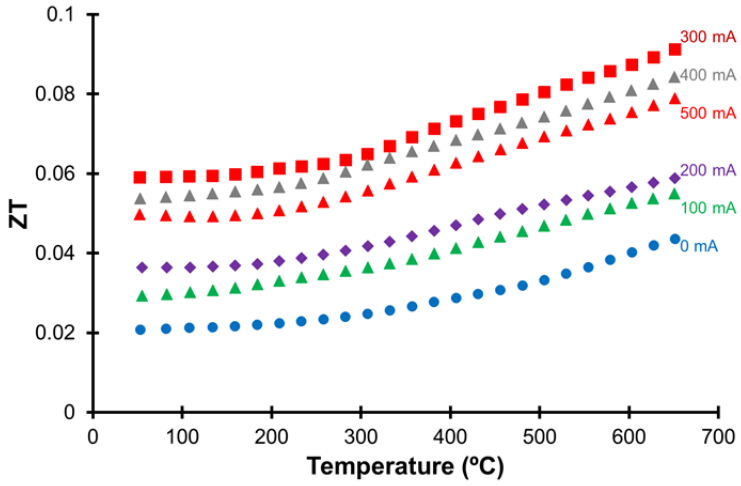

Fig. 12. ZT evolution with temperature for annealed samples grown with different external DC intensities.

Table 5. Reported values of thermoelectric parameters in literature and the ones obtained in the present work for BiSrCoO.

Preparation method	Resistance (mΩ cm)	Seebeck (μV/K)	PF (mW/K²m)	κ (W/(m K))	ZT	Ref.
As-grown fibres	8.7	142	0.2	-	-	[present work]
Annealed fibres	13	175	0.23	2.87 (RT)	0.09 (650 °C)	
Sinter-forged textured materials	40	150-205	0.05-0.20	0.5 - 2	0.1 (700 °C)	[30,32]
Sintered specimens under oxygen	15	170	0.19	2-4 (800 °C)	0.12 (800 °C)	[31]
Conventional sintering	12-160	90-170	0.03-0.16	0.9 -2.25 (RT-750 °C)	0.004-0.25 (RT-750 °C)	[36–40]

It should be also mentioned that the electric and thermoelectric values obtained in the present work are close or even better than the reported in the literature in the Bi-Sr-Co-O system (Table 2). However, it should be highlighted that most of the referenced samples are sintered materials, which should be subsequently processed to obtain the final shapes for their integration into TE modules, while EALFZ processing provides materials with the final shape in just one step. Some future-planned experiments envisage the modification of the electrical current waveform to decrease thermal conductivity.

4. Conclusions

This work demonstrates that $Bi_2Sr_2Co_{1.8}O_y$ thermoelectric materials can be directionally grown by the Electrically Assisted Laser Floating Zone method (EALFZ). The growth process leads to multiphasic textured bulk materials, with characteristics which are strongly dependent on the sign and intensity of the applied electrical DC. It has been found that negative currents hinder the formation of the thermoelectric phase, while positive ones promote the decrease of secondary phases number and content when

compared with samples grown without current. On the other hand, annealed samples present a lower amount of secondary phases and higher orientation than the as-grown ones, leading to higher TE performances. The highest ZT values (0.09) have been determined at 650 °C in +300 mA grown samples. Despite this relatively low value, when compared to doped materials in this family, it is important to highlight that samples prepared through the EALFZ process can be directly integrated on TE modules, avoiding long and expensive processes to shape the components for integration in TE devices. Other methods of applying EALFZ process are also considered for the future such as changing the waveform and/or frequency of the applied current.

Acknowledgements

Authors acknowledge the support of i3N (UIDB/50025/2020 & UIDP/50025/2020) and CICECO-Aveiro Institute of Materials (UID/CTM/50011/2020), financed by FCT/MEC and FEDER under the PT2020 Partnership Agreement.

This work is funded by national funds (OE), through FCT – Fundação para a Ciência e a Tecnologia, I.P., in the scope of the framework contract foreseen in the numbers 4, 5 and 6 of the article 23, of the Decree-Law 57/2016, of August 29, changed by Law 57/2017, of July 19.

A. Sotelo, M. A. Madre, and M. A. Torres acknowledge the MINECO-FEDER (MAT2017-82183-C3-1-R), and the Gobierno de Aragon (Grupo de Investigacion T 54-17 R) for funding.

References

[1] M.H. Elsheikh, D.A. Shnawah, M.F.M. Sabri, S.B.M. Said, M.H. Hassan, M.B.A. Bashir, M. Mohamad, A review on thermoelectric renewable energy: Principle parameters that affect their performance, Renew. Sust. Energ. Rev. 30 (2014) 337–355, https://doi.org/10.1016/j.rser.2013.10.027.

[2] H.C. Wang, J. Hwang, M.L. Snedaker, I.-H. Kim, C. Kang, J. Kim, G.D. Stucky, J. Bowers, W. Kim, High Thermoelectric Performance of a Heterogeneous PbTe Nanocomposite, Chem. Mater. 27 (2015) 944–999, https://doi.org/10.1021/cm5042138.

[3] D.M. Rowe, Thermoelectrics Handbook: Macro to Nano, 1st ed, CRC Press, Boca Raton, FL, 2006, pp. 1-3–1-7.

[4] I. Terasaki, Y. Sasago, K. Uchinokura, Large thermoelectric power in $NaCo_2O_4$ single crystals, Phys. Rev. B 56 (1997) 12685, https://doi.org/10.1103/PhysRevB.56.R12685.

[5] A. Sotelo, Sh. Rasekh, G. Constantinescu, M.A. Torres, M.A. Madre, J.C. Diez, Improvement of textured $Bi_{1.6}Pb_{0.4}Sr_2Co_{1.8}O_x$ thermoelectric performances by metallic

Ag additions, Ceram. Int. 39 (2013) 1597–1602, https://doi.org/10.1016/j.ceramint.2012.07.112.

[6] M. Abdellahi, M. Bahmanpour, M. Bahmanpour, Modeling Seebeck coefficient of $Ca_{3-x}M_xCo_4O_9$ (M=Sr, Pr, Ga, Ca, Ba, La, Ag) thermoelectric ceramics, Ceram. Int. 41 (2015) 345–352, https://doi.org/10.1016/j.ceramint.2014.08.077.

[7] K. Rubesova, T. Hlasek, V. Jakes, S. Huber, J. Hejtmanek, D. Sedmidubsky, Effect of a powder compaction process on the thermoelectric properties of $Bi_2Sr_2Co_{1.8}O_x$ ceramics, J. Eur. Ceram. Soc. 35 (2015) 525–531, https://doi.org/10.1016/j.jeurceramsoc.2014.08.037.

[8] Y.H. Zhu, W.B. Su, J. Liu, Y.C. Zhou, J. Li, X. Zhang, Y. Du, C.L. Wang, Effects of Dy and Yb co-doping on thermoelectric properties of $CaMnO_3$ ceramics, Ceram. Int. 41 (2015) 1535–1539, https://doi.org/10.1016/j.ceramint.2014.09.089.

[9] A. Sotelo, M.A. Torres, M.A. Madre, J.C. Diez, Effect of synthesis process on the densification, microstructure, and electrical properties of $Ca_{0.9}Yb_{0.1}MnO_3$ ceramics, Int. J. Appl. Ceram. Technol. 14 (2017) 1190–1196, https://doi.org/10.1111/ijac.12711.

[10] J. Liu, C.L. Wang, Y. Li, W.B. Su, Y.H. Zhu, J.C. Li, L.M. Mei, Influence of rare earth doping on thermoelectric properties of $SrTiO_3$ ceramics, J. Appl. Phys. 114 (2013) 223714, https://doi.org/10.1063/1.4847455.

[11] A. Maignan, S. Hébert, M. Hervieu, C. Michel, D. Pelloquin, D. Khomskii, Magnetoresistance and magnetothermopower properties of Bi/Ca/Co/O and Bi(Pb)/Ca/Co/O misfit layer cobaltites, J Phys: Condens Matter 15 (2003) 2711–2723, https://doi.org/10.1088/0953-8984/15/17/323.

[12] H. Wang, X. Sun, X. Yan, D. Huo, X. Li, J.-G. Li, X. Ding, Fabrication and thermoelectric properties of highly textured $Ca_9Co_{12}O_{28}$ ceramic, J. Alloys Compds. 582 (2014) 294–298, https://doi.org/10.1016/j.jallcom.2013.07.145.

[13] Sh. Rasekh, F.M. Costa, N.M. Ferreira, M.A. Torres, M.A. Madre, J.C. Diez, A. Sotelo, Use of laser technology to produce high thermoelectric performances in $Bi_2Sr_2Co_{1.8}O_x$, Mater. Design 75 (2015) 143–148, https://doi.org/10.1016/j.matdes.2015.03.005.

[14] J.G. Noudem, D. Kenfaui, D. Chateigner, M. Gomina, Toward the enhancement of thermoelectric properties of lamellar $Ca_3Co_4O_9$ by edge-free spark plasma texturing, Scr. Mater. 66 (2012) 258–260, https://doi.org/10.1016/j.scriptamat.2011.11.004.

[15] M.A. Madre, F.M. Costa, N.M. Ferreira, S.I.R. Costa, Sh. Rasekh, M.A. Torres, J.C. Diez, V.S. Amaral, J.S. Amaral, A. Sotelo, High thermoelectric performance in $Bi_{2-x}Pb_xBa_2Co_2O_y$ promoted by directional growth and annealing, J. Eur. Ceram. Soc. 36 (2016) 67–74, https://doi.org/10.1016/j.jeurceramsoc.2015.09.034.

[16] H.Y. Choi, M.H. Lee, S.M. Choi, W.S. Seo, H.L. Lee, Effect of the reactive template particle size on the thermoelectric property of $Ca_3Co_4O_9$ oxide with the RTGG and SPS process, J. Ceram. Proc. Res. 13 (2012) S114–S118.

[17] N.M. Ferreira, Sh. Rasekh, F.M. Costa, M.A. Madre, A. Sotelo, J.C. Diez, M.A. Torres, New method to improve the grain alignment and performance of thermoelectric ceramics, Mater. Lett. 83 (2012) 144–147, https://doi.org/10.1016/j.matlet.2012.05.131.

[18] B. Liu, X. Liu, P. Li, F. Li, B. Shen, J. Zhai, Improving piezoelectric properties by controlling phase structure and crystal orientation, RSC Adv. 7 (2017) 41788, https://doi.org/10.1039/c7ra07711d.

[19] Sh. Rasekh, N.M. Ferreira, F.M. Costa, G. Constantinescu, M.A. Madre, M.A. Torres, J.C. Diez, A. Sotelo, Development of a new thermoelectric $Bi_2Ca_2Co_{1.7}O_x$ + $Ca_3Co_4O_9$ composite, Scr. Mater. 80 (2014) 1–4, https://doi.org/10.1016/j.scriptamat.2014.01.032.

[20] F.M. Costa, N.M. Ferreira, Sh. Rasekh, A.J.S. Fernandes, M.A. Torres, M.A. Madre, J.C. Diez, A. Sotelo, Very large superconducting currents induced by growth tailoring, Cryst. Growth Des. 15 (2015) 2094–2101, https://doi.org/10.1021/cg5015972.

[21] R. Funahashi, I. Matsubara, S. Sodeoka, Thermoelectric properties of $Bi_2Sr_2Co_2O_x$ polycrystalline materials, Appl. Phys. Lett. 76 (2000) 2385–2387, https://doi.org/10.1063/1.126354.

[22] J.J. Shen, X.X. Liu, T.J. Zhu, X.B. Zhao, Improved thermoelectric properties of La-doped $Bi_2Sr_2Co_2O_9$-layered misfit oxides, J. Mater. Sci. 44 (2009) 1889–1893, https://doi.org/10.1007/s10853-009-3279-0.

[23] E. Combe, R. Funahashi, F. Azough, R. Freer, Relationship between microstructure and thermoelectric properties of $Bi_2Sr_2Co_2O_x$ bulk materials, J. Mater. Res. 29 (2014) 1376–1382, https://doi.org/10.1557/jmr.2014.135.

[24] R. Funahashi, M. Shikano, $Bi_2Sr_2Co_2O_y$ whiskers with high thermoelectric figure of merit, Appl. Phys. Lett. 81 (2002) 1459, https://doi.org/10.1063/1.1502190.

[25] M. Jost, J. Lingner, M. Letz, G. Jakob, Thermoelectric properties of p-type $Bi_2Sr_2Co_2O_9$ glass-ceramics, Semicond. Sci. Technol. 29 (2014) 124011, https://doi.org/10.1088/0268-1242/29/12/124011.

[26] A. Sotelo, M.A. Torres, G. Constantinescu, Sh. Rasekh, J.C. Diez, M.A. Madre, Effect of Ag addition on the mechanical and thermoelectric performances of annealed $Bi_2Sr_2Co_{1.8}O_x$ textured ceramics, J. Eur. Ceram. Soc. 32 (2012) 3745–3751, https://doi.org/10.1016/j.jeurceramsoc.2012.05.035.

[27] O. Jankovský, D. Sedmidubský, Phase equilibria modelling in Bi–Sr–Co–O system—Towards crystal growth and melt-assisted material processing, J. Eur. Ceram. Soc. 38 (2018) 131–135, https://doi.org/10.1016/j.jeurceramsoc.2017.08.035.

[28] M.F. Carrasco, R.F. Silva, J.M. Vieira, F.M. Costa, Electrical field freezing effect on laser floating zone (LFZ)-grown $Bi_2Sr_2Ca_2Cu_4O_{11}$ superconducting fibres, Supercond. Sci. Technol. 17 (2004) 612–619, https://doi.org/10.1088/0953-2048/17/4/008.

[29] J.C. Diez, E. Guilmeau, M.A. Madre, S. Marinel, S. Lemonnier, A. Sotelo, Improvement of $Bi_2Sr_2Co_{1.8}O_x$ thermoelectric properties by laser floating zone texturing, Solid State Ionics 180 (2009) 827–830, https://doi.org/10.1016/j.ssi.2009.02.004.

[30] W. Shin, N. Murayama, Thermoelectric properties of (Bi,Pb)-Sr-Co-O oxide, J Mater Res 15 (2000) 382–386, https://doi.org/10.1557/JMR.2000.0060.

[31] H. Itahara, C. Xia, J. Sugiyama, T. Tani, Fabrication of textured thermoelectric layered cobaltites with various rock salt-type layers by using β-$Co(OH)_2$ platelets as reactive templates, J Mater Chem 14 (2004), https://doi.org/10.1039/B309804D61-6.

[32] M.A. Madre, Sh. Rasekh, J.C. Diez, A. Sotelo, New solution method to produce high performance thermoelectric ceramics: a case study of Bi-Sr-Co-O, Mater Lett 64 (2010) 2566–2568, https://doi.org/10.1016/j.matlet.2010.08.041.

[33] M.A. Madre, F.M. Costa, N.M. Ferreira, S.I.R. Costa, Sh. Rasekh, M.A. Torres, J.C. Diez, V.S. Amaral, J.S. Amaral, A. Sotelo, High thermoelectric performance in $Bi_{2-x}Pb_xBa_2Co_2O_y$ promoted by directional growth and annealing, J Eur Ceram Soc 36 (2016) 67–74, https://doi.org/10.1016/j.jeurceramsoc.2015.09.034.

[34] G.Ç. Karakaya, B. Özçelik, M.A. Torres, M.A. Madre, A. Sotelo, Effect of Na-doping on thermoelectric and magnetic performances of textured $Bi_2Sr_2Co_2O_y$ ceramics, Journal of the European Ceramic Society 38 (2018) 515–520, https://doi.org/10.1016/j.jeurceramsoc.2017.09.006.

[35] M.E. Fine, N. Hsieh, Wiedermann-Franz-Lorenz relation in highly electronic-conducting oxides, J. Am. Ceram. Soc. 57 (1974) 502–503.

[36] L.H. Yin, R. Ang, B.C. Zhao, Y.N. Huang, Y. Liu, S.G. Tan, W.H. Song, Y.P. Sun, Evolution of the thermoelectric performance in low Ca-doped layered cobaltite $Bi_2Sr_2Co_2O_y$, Solid State Communications 158 (2013) 16–19, https://doi.org/10.1016/j.ssc.2013.01.002.

[37] C. Boyle, P. Carvillo, Y. Chen, E.J. Barbero, D. Mcintyre, X. Song, Grain boundary segregation and thermoelectric performance enhancement of bismuth doped calcium cobaltite, Journal of the European Ceramic Society 36 (2016) 601–607, https://doi.org/10.1016/j.jeurceramsoc.2015.10.042.

[38] Y. Huang, B. Zhao, S. Lin, Y. Sun, Optimization of thermoelectric properties in layered $Bi_2Sr_2Co_2O_y$ via high-magnetic-field sintering, Journal of Alloys and Compounds 705 (2017) 745–748, https://doi.org/10.1016/j.jallcom.2017.02.104.

[39] Z. Diao, H.N. Lee, M.F. Chisholm, R. Jin, Thermoelectric properties of $Bi_2Sr_2Co_2O_y$ thin films and single crystals, Physica B: Condensed Matter 511 (2017) 42–46, https://doi.org/10.1016/j.physb.2017.02.001.

[40] S. Wang, Z. Bai, H. Wang, Q. Lü, J. Wang, G. Fu, High temperature thermoelectric properties of $Bi_2Sr_2Co_2O_y$/Ag composites, Journal of Alloys and Compounds 554 (2013) 254–257, https://doi.org/10.1016/j.jallcom.2012.11.107.